Full-waveform inversion for full-wavefield imaging: Decades in the making

Rongxin Huang[1], Zhigang Zhang[1], Zedong Wu[1], Zhiyuan Wei[1], Jiawei Mei[1], and Ping Wang[1]

Abstract

Seismic imaging using full-wavefield data that includes primary reflections, transmitted waves, and their multiples has been the holy grail for generations of geophysicists. To be able to use the full-wavefield data effectively requires a forward-modeling process to generate full-wavefield data, an inversion scheme to minimize the difference between modeled and recorded data, and, more importantly, an accurate velocity model to correctly propagate and collapse energy of different wave modes. All of these elements have been embedded in the framework of full-waveform inversion (FWI) since it was proposed three decades ago. However, for a long time, the application of FWI did not find its way into the domain of full-wavefield imaging, mostly owing to the lack of data sets with good constraints to ensure the convergence of inversion, the required compute power to handle large data sets and extend the inversion frequency to the bandwidth needed for imaging, and, most significantly, stable FWI algorithms that could work with different data types in different geologic settings. Recently, with the advancement of high-performance computing and progress in FWI algorithms at tackling issues such as cycle skipping and amplitude mismatch, FWI has found success using different data types in a variety of geologic settings, providing some of the most accurate velocity models for generating significantly improved migration images. Here, we take a step further to modify the FWI workflow to output the subsurface image or reflectivity directly, potentially eliminating the need to go through the time-consuming conventional seismic imaging process that involves preprocessing, velocity model building, and migration. Compared with a conventional migration image, the reflectivity image directly output from FWI often provides additional structural information with better illumination and higher signal-to-noise ratio naturally as a result of many iterations of least-squares fitting of the full-wavefield data.

Introduction

For decades, seismic imaging — the process of obtaining a reflectivity model representing the structural image of the subsurface — has relied mainly on migration. Seismic migration is accomplished by extrapolating source and receiver wavefields into the subsurface using a given velocity model and estimating the reflectivity model at each subsurface grid point by applying an imaging condition (e.g., cross-correlation, deconvolution) to the incident and reflected wavefields. Since the inception of the imaging principle (Claerbout, 1971), migration has been at the heart of seismic research (e.g., Loewenthal et al., 1976; Baysal et al., 1983; Nemeth et al., 1999) and a key step in seismic imaging.

As a good velocity model is required to properly propagate and focus the wavefields, velocity model building (VMB) is also an essential step in seismic imaging. This is often a challenging task, especially in areas with complex geology and poor data constraints. Moreover, since conventional migration algorithms can only handle single-scattering energy, the input data to migration must be prepared to meet such a requirement. Therefore, the other key step of seismic imaging is preprocessing, of which the main goal, in addition to improving the signal-to-noise ratio (S/N) of the data, is to retain only the primary reflections by attenuating the rest of the energy from the full-wavefield data through steps such as deghosting and demultiple (Verschuur et al., 1992; Wang et al., 2013). These steps are not only time consuming but also very difficult as completely removing the targeted "noise" without damaging the primary signals is often challenging. More importantly, a significant part of the full-wavefield data that could otherwise provide additional illumination to the subsurface is discarded after preprocessing.

Attempts to use other parts of the wavefield, in addition to primary reflections, for imaging include migration of multiples. This utilizes surface multiples as signals and thus improves the subsurface illumination compared to primary migration because all receivers are turned into secondary sources and all orders of multiples can contribute to the subsurface imaging (Liu et al., 2010; Lu et al., 2011). However, migration of multiples is limited to surface multiples only, which also demands a good separation of primaries and surface multiples, and generally suffers from crosstalk noise among primaries and different orders of multiples (Yang et al., 2015). Wong et al. (2014) propose to use least-squares migration (LSM) of multiples to mitigate the crosstalk noise through an iterative least-squares data-fitting process. However, such approaches use Born modeling that only simulates single-scattering energy and still require a good separation of primaries and different orders of multiples.

Full-wavefield migration (FWM), proposed by Berkhout (2012), avoids the requirement of separating primaries and multiples. It uses an estimated reflectivity model to generate the full-wavefield response and iteratively updates the reflectivity model by minimizing the misfit between modeled and recorded full-wavefield data. As an accurate velocity model is essential for reconciling wavefields of different paths and minimizing potential crosstalk noise, FWM can be combined with a form of full-waveform inversion (FWI) into the so-called joint-migration-inversion (JMI) approach that iteratively updates both reflectivity and velocity models (Berkhout, 2012). However, both FWM and JMI use a one-way extrapolator as the modeling engine and

---

[1]CGG, Houston, Texas, USA. E-mail: rongxin.huang@cgg.com; zhigang.zhang@cgg.com; zedong.wu@cgg.com; zhiyuan.wei@cgg.com; jiawei.mei@cgg.com; ping.wang@cgg.com.

Special Section: Seismic imaging below complex overburdens

therefore cannot properly handle diving waves, which is the most important energy in the recorded data to update the velocity model and consequently improve focusing of the reflectivity model.

FWI, originally proposed by Lailly (1983) and Tarantola (1984), is a more elegant and natural way to handle full-wavefield data with a proper modeling engine that can generate all of the wave modes, including diving waves, primaries, and surface and internal multiples. A few years after FWI was proposed, Tarantola (1986) predicted that "Interpretation of industrial seismic data using inverse methods will probably become routine, and the stack-plus-migration method will become an ancient technique." However, after more than 30 years, Tarantola's prediction has not come true. There are two fundamental barriers preventing FWI from routinely producing directly interpretable images of the earth's subsurface: (1) the lack of a consistent FWI scheme that is effective for different data types and geologic settings and (2) the prohibitive computational requirement that made FWI unaffordable for years, especially for large apertures (needed for large offsets for deep diving-wave penetration) and high frequencies (needed for high resolution for seismic interpretation) (Zhang et al., 2020). Advancements in high-performance computing and recent progress in FWI algorithms to tackle problems such as cycle skipping and amplitude mismatch have widened FWI applications to include different data types, from ocean-bottom node (OBN) or ocean-bottom cable to wide-azimuth and narrow-azimuth towed-streamer data (WATS and NATS), and different geologic settings, from deep water to shallow water and offshore to onshore (Shen et al., 2017; Zhang et al., 2018; Wang et al., 2019). Though FWI has significantly simplified the VMB step, FWI is, to date, still mostly used to provide a velocity model for migration purposes, and seismic imaging is still bound by lengthy preprocessing and migration steps.

With an FWI algorithm that is effective for most cases, we take a step further to modify the FWI workflow to output the subsurface image or reflectivity directly. This potentially eliminates the need to go through the time-consuming seismic imaging process that involves preprocessing, VMB, and migration. Compared to conventional migration images, the reflectivity image directly output from FWI often provides additional structural information with more balanced illumination and higher S/N since FWI is a least-squares data-fitting process of the full-wavefield data, including diving waves and multiples.

FWI imaging

FWI and migration share the same goal of accurately describing the interior of the earth, but they have two distinct views of the problem. In principle, inversion includes migration and potentially solves for velocity and migration (reflectivity) in one go (Etgen et al., 2009). However, it cannot serve as a self-contained processing workflow unifying macromodel building and migration if it is limited to low frequencies (Virieux and Operto, 2009) because high frequencies are needed for the high-resolution migration image.

A successful migration application beneath a complex overburden requires a fairly accurate velocity model to produce a well-focused image. FWI has not always been able to competently deliver such a velocity model until recently, especially for salt

settings (Michell et al., 2017; Shen et al., 2017; Zhang et al., 2018; Wang et al., 2019). Time-lag FWI (TLFWI) mitigates the cycle skipping and amplitude-discrepancy issues between synthetic data and recorded seismic data (Zhang et al., 2018) with a kinematics-only cost function as follows:

$$\chi(v) = \sum_{s,r,w} c\Delta\tau^2 , \qquad (1)$$

where v is the velocity model, c is a cross-correlation coefficient, w is the window index, $\Delta\tau$ is the time shift between the recorded data and synthetic data, and s and r are the source and receiver index, respectively. For details about gradient computation, please refer to equation 5 in Zhang et al. (2018).

Wang et al. (2019) demonstrate that high-frequency FWI gives fine details in the velocity model but with negligible impact on the kinematics and the corresponding migration images. Meanwhile, there have been proposals to directly interpret the high-frequency FWI velocity model (Sirgue et al., 2009; Lu, 2016; Shen et al., 2018a). Nevertheless, velocity and reflectivity represent the subsurface model from different perspectives. The reflectivity is defined as the volumetric distribution of reflection coefficients. At normal incidence, the reflection coefficient is the normalized impedance contrast, and the impedance contrast across the interface can be obtained by

$$\frac{\partial I}{\partial n} = \frac{\partial I}{\partial x}\sin\theta\cos\varphi + \frac{\partial I}{\partial y}\sin\theta\sin\varphi + \frac{\partial I}{\partial z}\cos\theta , \qquad (2)$$

where the impedance is the multiplication of density and velocity, $I = \rho v$, and θ and φ are dip angle and azimuth angle of the normal vector to the subsurface reflectors, which can be obtained by automatically scanning through the velocity model. In this paper, we assume density is a constant or a smooth function and only focus on the relationship between reflectivity and velocity (note that any other velocity-to-density relationship could be used). Then, the impedance contrast can be approximated as

$$\frac{\partial I}{\partial n} \approx \rho\left(\frac{\partial v}{\partial x}\sin\theta\cos\varphi + \frac{\partial v}{\partial y}\sin\theta\sin\varphi + \frac{\partial v}{\partial z}\cos\theta\right). \qquad (3)$$

FWI as described in equation 1 can then be modified to also output the reflectivity model following equation 3. We hereinafter refer to this approach as "FWI imaging" and the resulting reflectivity model as an "FWI image" (Zhang et al., 2020).

Field data examples

Equation 3 indicates that FWI imaging is essentially still FWI but with an output of the zero-angle reflectivity in the structural normal direction. It has been demonstrated that TLFWI is able to improve the velocity model for different data types and in different geologic settings. While the TLFWI velocity model is often used as the migration velocity to improve conventional

migration images such as Kirchhoff, reverse time migration (RTM), Q-compensated reverse time migration (Q-RTM), and least-squares reverse time migration (LSRTM), it is of high interest to compare those images with the direct output of FWI imaging.

Atlantis OBN in the Gulf of Mexico. The Atlantis Field is one of the largest oil fields in the Gulf of Mexico (GoM), lying directly below the Sigsbee Escarpment where the water depth changes rapidly from approximately 1.5 km to approximately 2.3 km within a short distance. A significant portion of the field is shadowed by a complex allochthonous salt body with several thin salt fingers, which for a long time has made it nearly impossible to image the subsalt reservoir using the conventional VMB workflow driven by manual salt interpretation (Roberts et al., 2011). In 2014–2015, a wider-offset OBN survey was acquired with the aim of facilitating VMB in addition to its normal reservoir monitoring task (Lewis et al., 2016). This OBN data set has good low frequencies down to 1.5 Hz and long offsets up to 30 km, which is deemed as one of the key elements for the successful application of FWI for automated salt model building, in addition to a good initial model and a proper FWI algorithm (Shen et al., 2018b). As shown in Figure 1b, TLFWI, starting from a smoothed legacy model (Figure 1a) built by the conventional workflow, was able to significantly remodel the complex salt geometry and resolve details in the sediment velocity, especially in areas close to the salt body. This led to considerable improvements in the RTM image (Figure 1d), from directly below the shallow salt body to the base of the Louann salt, when compared to the legacy RTM image

(Figure 1c). However, for the subsalt reservoir, there are still considerable migration swings and noise, and event continuity is still suboptimal, as indicated by the yellow ellipse in Figure 1d. This smear zone directly below the complex salt fingers in the RTM image can be better observed in the perpendicular direction, as shown in Figures 2b and 2d. Is this due to residual velocity errors or illumination deficiency? The FWI image corresponding to the 18 Hz FWI velocity model gives better-defined subsalt structures with much-improved event continuity and S/N, as well as more balanced amplitudes (Figures 2c and 2e), indicating that velocity errors are less of a problem in this area than illumination issues since the migration velocity of RTM (Figures 2b and 2d) is the same 18 Hz FWI velocity. We also observed that the FWI image can extend the image to a broader region at the survey boundary (arrows in Figures 2b and 2c). There are three major differences between RTM (migrated with FWI velocity) and FWI imaging: input data, modeling, and imaging procedure. RTM takes processed primary reflections as input, and the modeling does not simulate multiples and the rest of the wavefield. By contrast, FWI imaging uses raw data with all recorded signals including transmissions, reflections, and both primaries and multiples. The extra input energy offers additional illumination that infills illumination holes and extends the coverage at the survey boundary (arrow in Figure 2c). As for the imaging procedure, the RTM image is obtained through an adjoint operator whereas the FWI image is the result of an iterative least-squares data-fitting process, which has similar benefits to LSM, such as
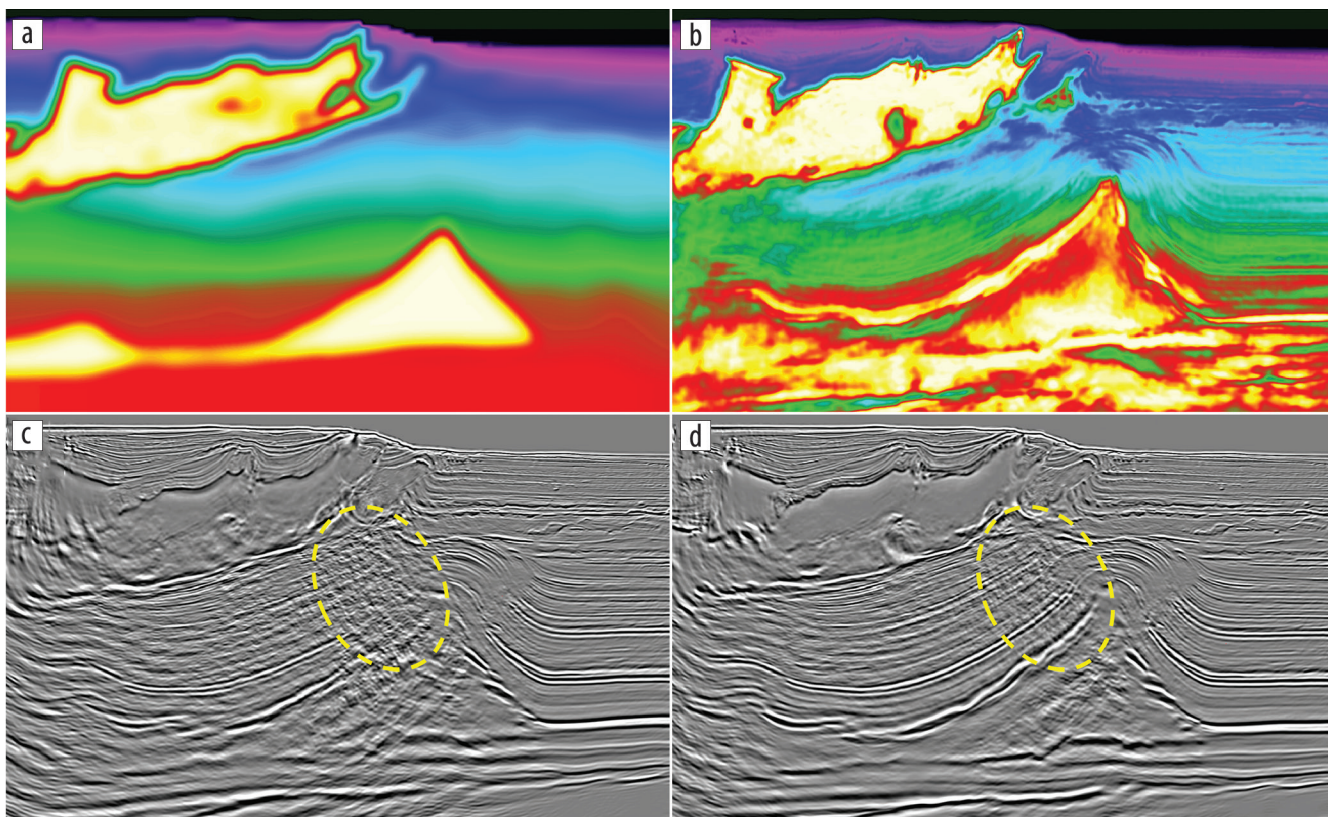

Figure 1. Inline section of (a) the TLFWI input model from the smoothed legacy velocity and (b) the 18 Hz TLFWI model, and their corresponding 18 Hz RTM images migrated with Atlantis OBN data (c) and (d). TLFWI resolves the complex velocity details in the overburden, especially the salt geometry, and greatly improves the subsalt image.

Special Section: Seismic imaging below complex overburdens

balancing illumination and mitigating migration artifacts on the images. We believe that both the input data and the imaging procedure have contributed to the difference between the FWI image and the RTM image (Zhang et al., 2020).

The difference can also be seen on a depth slice at the reservoir level. On the RTM image (Figure 3a), the area directly below the complex salt fingers is obscured by noise (yellow circle in Figure 3a), and the faults are barely noticeable (yellow arrow in Figure 3a). On the FWI image (Figure 3b), the structures within the yellow circle are more continuous and the faults are better defined, which is likely because of the effect of the least-squares data fitting that enhances the illumination and suppresses

migration artifacts, as well as the additional illumination from the rest of the wavefield beyond primary reflections. Although the FWI image generally appears to have a higher S/N, noise in the input data and crosstalk noise caused by multiples during the FWI gradient computation could be mapped into the FWI velocity model and in turn into the FWI image. Furthermore, some events in the FWI image may be artificial because of the simplified physics of the acoustic wave propagation engine and the inversion algorithm, which cannot account for all the recorded energy (Zhang et al., 2020).

Walker Ridge WATS in the GoM. Similar benefits from FWI imaging over RTM can be observed in another salt province at
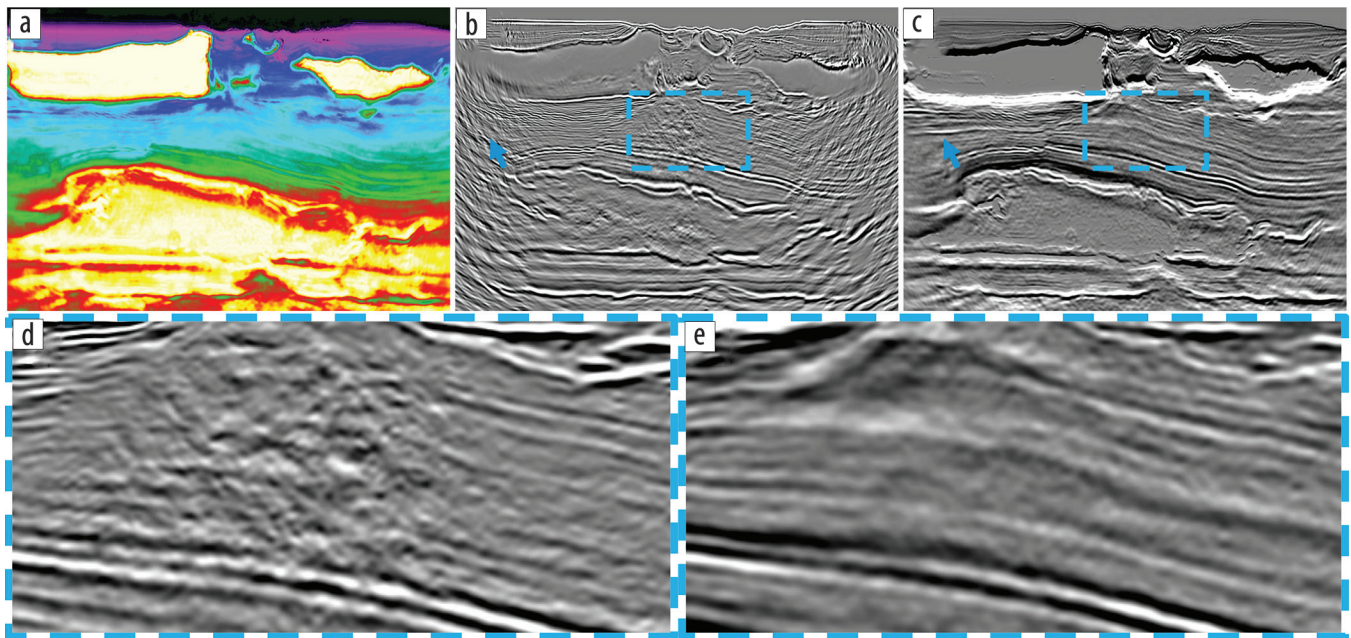

Figure 2. Crossline section of Atlantis OBN. (a) The 18 Hz TLFWI model, (b) its corresponding 18 Hz RTM image, and (c) the 18 Hz FWI image. Panels (d) and (e) are the zoomed-in sections of the blue rectangles in (b) and (c), respectively.
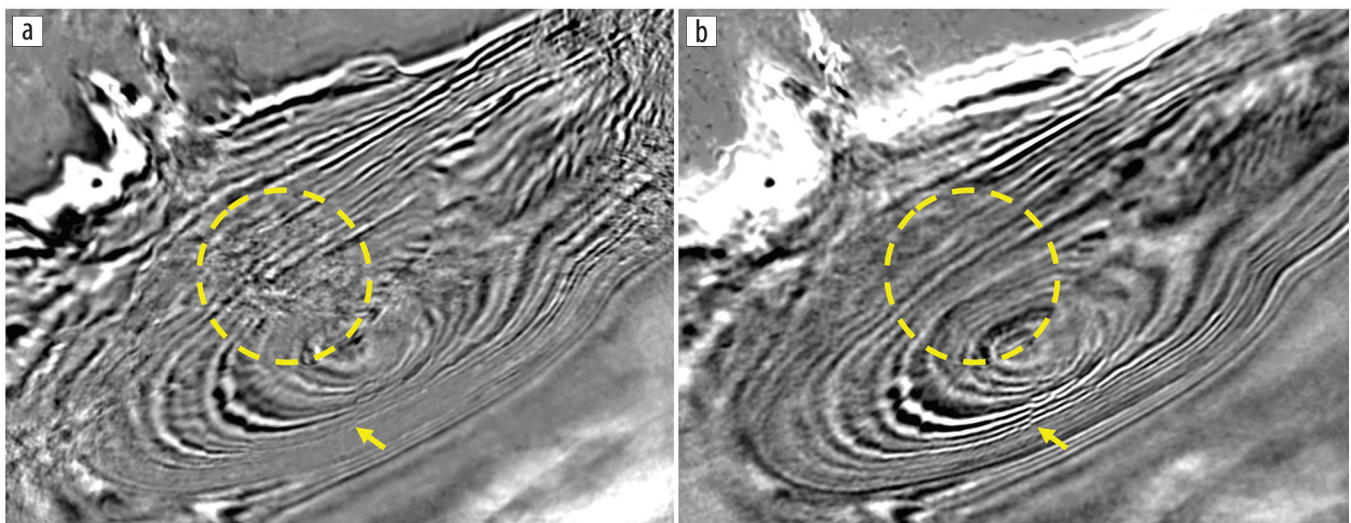

Figure 3. Depth slice of Atlantis OBN. (a) The 18 Hz RTM image migrated with the 18 Hz TLFWI model and (b) the 18 Hz FWI image. The area indicated by the yellow circle is directly below complex salt fingers and has a low illumination. In this region, the FWI image shows a much-improved coherency and S/N over the RTM image. The yellow arrow points to faults that are better defined in the FWI image.

Special Section: Seismic imaging below complex overburdens

Walker Ridge, GoM, with a similar level of salt complexity but a much less FWI-friendly data set compared to the previous example. The salt in the Walker Ridge area is characterized by thick and tabular salt bodies with complex overhangs and protrusions at the front of movement and fed from below by salt pedestals connecting to the Louann mother salt. Quite a few discoveries, either four-way turtle structures below tabular salt or three-way truncations against the salt feeder, have been made in the last two decades, making it one of the most prospective areas in the GoM. The WATS data available for this study were acquired in 2008, with an inline offset of approximately 8 km and a crossline offset of approximately 2 km — about half the crossline offset of conventional WATS surveys. The limits of this WATS data are that the penetration depth of diving waves is limited to be above the regional base of salt or shallower depths and the useable low-frequency signal is only at 2.8 Hz and above. Compounded with the complex salt geometry, this makes it difficult to build a good velocity model for imaging with FWI. Nonetheless, TLFWI using this WATS data was still quite helpful in resolving the complex salt geometry at shallow depths and brought significant improvements to the subsalt image when compared to the legacy image. However, RTM with the TLFWI model still has poorly imaged areas, most notably directly below the complex salt (as indicated by the yellow arrow in Figure 4a) and at the three-way truncation against the salt feeder (as indicated by the yellow ellipse in Figure 4a). By contrast, the FWI image revealed the steeply dipping Paleogene and Cretaceous reflectors in the three-way truncation area (yellow ellipse in Figure 4b), suppressed the noise, and improved the event continuity in the area directly below the complex salt (yellow arrow in Figure 4b). Again, we attribute these improvements from the FWI image to the use of full-wavefield data and the least-squares data-fitting process that enhances the images in the still poorly illuminated areas, even with the full-wavefield data. We also note that the FWI image from WATS data is still noisy overall, despite its improvements over the RTM image, because WATS data are insufficient for FWI to resolve the velocity for such a complex structure, and the FWI image is only as good as the FWI velocity.
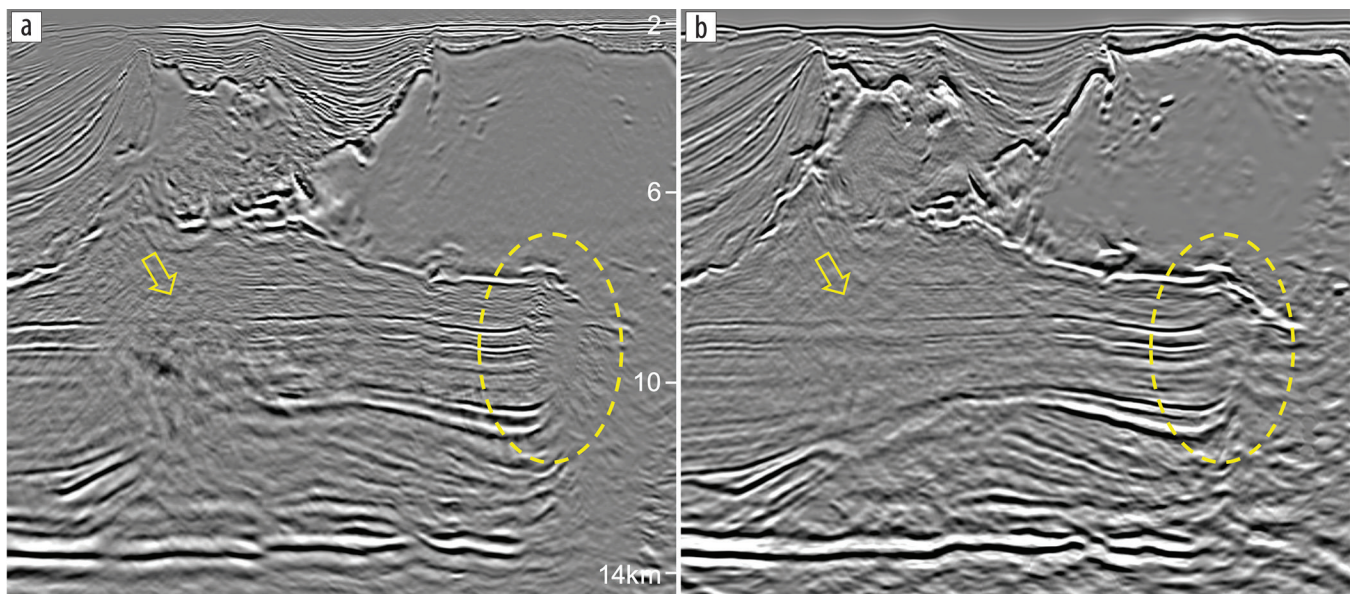

Figure 4. Section view of (a) the 15 Hz RTM image and (b) the 15 Hz FWI image from the corresponding 15 Hz TLFWI model for a WATS data set in Walker Ridge, GoM. The FWI image shows better event continuity in the areas right below complex salt (as indicated by the arrows) and at the steeply dipping three-way truncation (as highlighted by the ellipses).
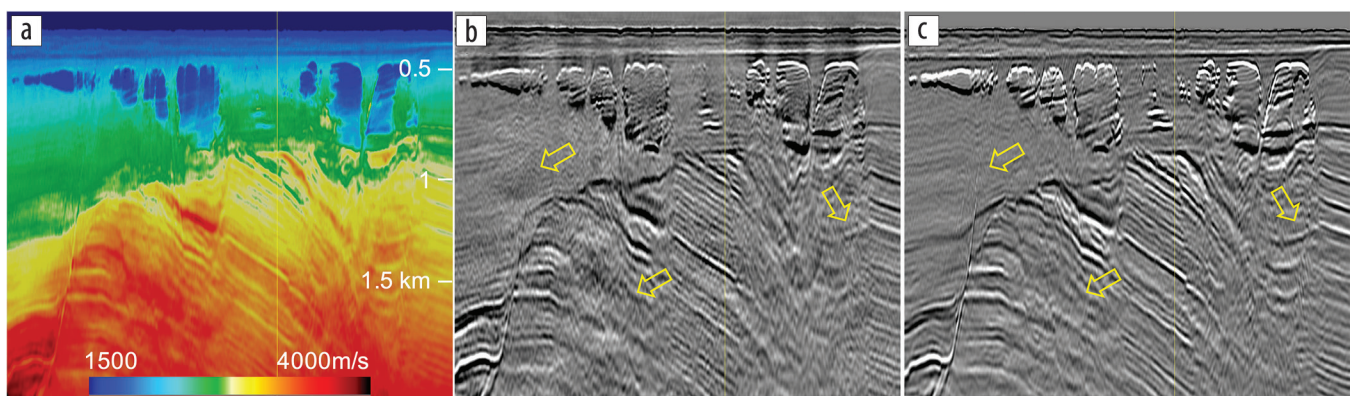

Figure 5. Section view of (a) the 40 Hz TLFWI model, (b) the 40 Hz Q-RTM, and (c) the 40 Hz FWI image from a source-over-spread NATS data set in the Barents Sea. Subgas reflectors and faults are better revealed in the FWI image in the areas indicated by the arrows.

Source-over-spread NATS in the Barents Sea. FWI imaging is not only effective for imaging subsalt, low-illumination areas but also for subgas zones where primary reflections suffer from strong attenuation. In the Barents Sea, shallow gas and gas hydrate anomalies are known challenges when imaging often highly faulted subgas shallow reservoirs, in addition to the hard and rugose sea floor in this region. To overcome such challenges in imaging shallow reservoirs, a source-over-spread acquisition was proposed on top of conventional NATS acquisition (Vinje et al., 2017), where a group of sources are placed at the center of the deep-towed spread to acquire the much-needed near offsets for shallow imaging while the front source in the conventional NATS survey is retained to provide long offsets up to 8.2 km for VMB. In 2019, such a survey was acquired in the Greater Castberg area with the aim of bringing significant uplifts to the seismic images over vintage data. As shown in Figure 5a, TLFWI up to 40 Hz can resolve the shallow gas clouds and deeper carbonate blocks in greater detail, providing significantly improved images over a major part of the survey area. However, Q-RTM images of subgas reflectors and faults in this local region are still quite poor (as indicated by yellow arrows in Figure 5b), even with a fairly good velocity model

and a reasonably estimated Q model, mainly because the primary reflections used as the input to Q-RTM suffer from strong attenuation when passing through the shallow gas clouds twice and leave barely any signals for imaging. In comparison, the FWI image gives much-improved images of subgas reflectors and faults with better continuity and S/N (Figure 5c). This is mostly because FWI imaging uses other parts of the wavefield, such as diving waves and multiples, some of which only pass through the gas clouds once or completely bypass them. The benefits of diving waves and multiples at infilling illumination gaps can be better seen on a shallow depth slice, where the 40 Hz FWI image (Figure 6c) provides greater details of shallow geologic features with less-obvious acquisition footprints compared to the 40 Hz Q-RTM (Figure 6b) and 100 Hz Q-Kirchhoff (Figure 6a) images.

Shallow-water OBN in Trinidad and Tobago. The power of FWI imaging in utilizing diving waves and multiples for shallow imaging is more clearly demonstrated on a shallow-water OBN data set in Trinidad and Tobago. This OBN survey was acquired in 2018 in an area with water depths ranging from 12 to 40 m. The node spacing is approximately 125–150 × 200 m and the shot spacing is 50 × 50 m. Due to platform obstruction and shallow
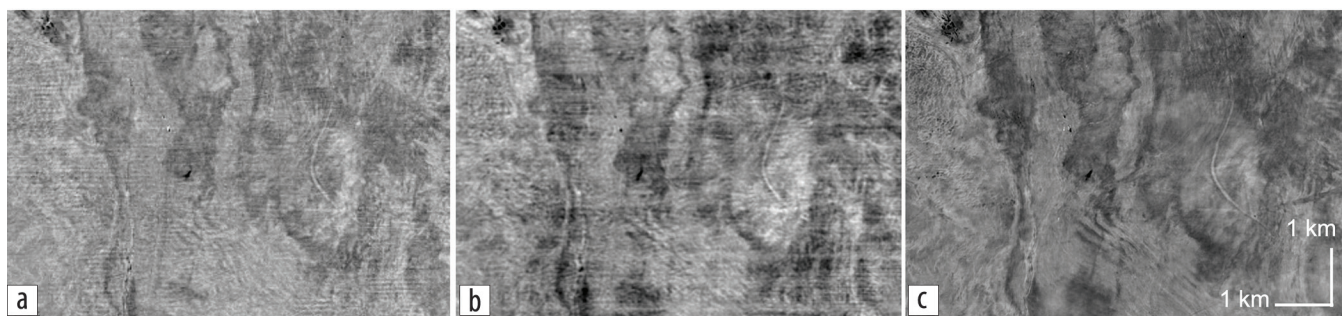

Figure 6. Depth slice at 390 m of (a) the 100 Hz Q-Kirchhoff, (b) the 40 Hz Q-RTM, and (c) the 40 Hz FWI image from the Barents Sea source-over-spread NATS data. The FWI image is free of acquisition footprints and provides greater details of shallow geologic features.
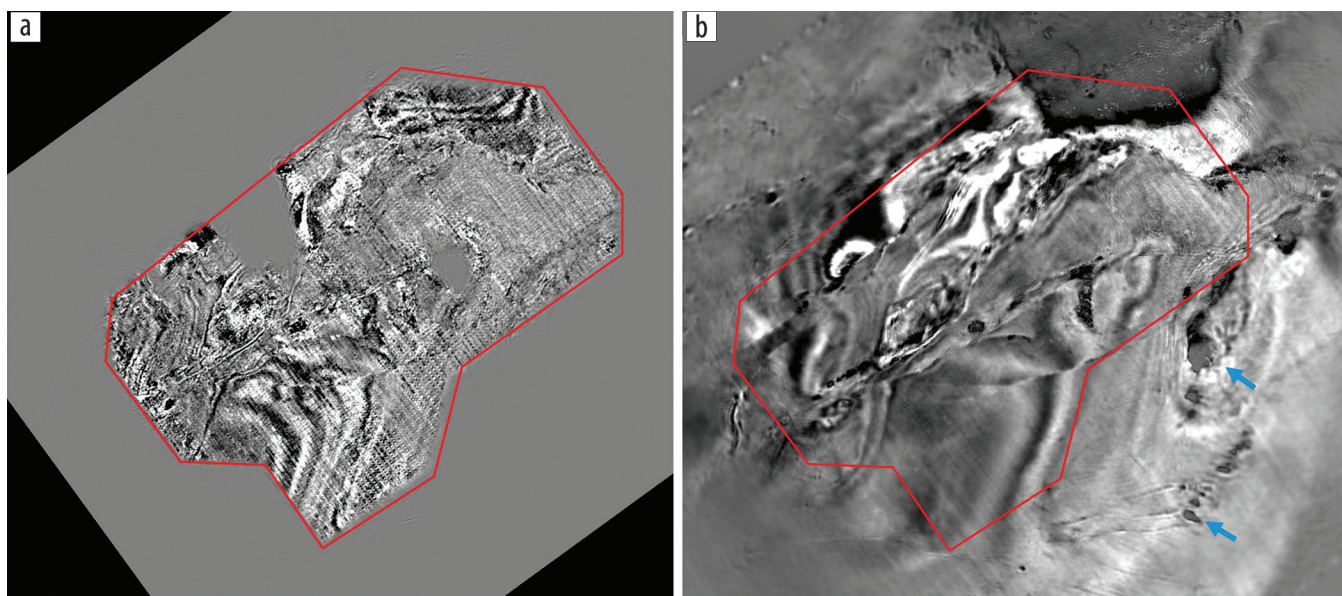

Figure 7. Depth slice at 200 m of (a) the 24 Hz RTM image and (b) the 24 Hz FWI image of a shallow-water OBN data set in Trinidad and Tobago. The red polygon indicates the node coverage, and the blue arrows point to small geobodies that are well resolved in the FWI image by diving waves and multiples outside the node coverage.

Special Section: Seismic imaging below complex overburdens

coral reefs, relatively large acquisition holes with missing shots or receivers, or both, are present in the survey, causing imaging holes in the RTM image as shown in Figure 7a. The FWI image seamlessly fills in the acquisition holes and extends the image from the node coverage to the shot coverage (Figure 7b). The shallow anomalies outside the node coverage are also well imaged with a resolution similar to those inside (blue arrows in Figure 7b). Besides infilling the illumination gaps, diving waves are particularly helpful for resolving the lateral velocity heterogeneity with their nearly horizontal kernel and therefore improving the lateral resolution of the TLFWI model and FWI image. Meanwhile, least-squares data fitting of the full-wavefield data leads to suppression of the acquisition footprint in this shallow-water area and reveals detailed geologic features that cannot be seen clearly on the RTM image.

Discussion

We have shown that FWI images offer an alternative view of the FWI velocity model akin to conventional migration images. They provide meaningful subsurface structure information and often superior images over conventional migrations in the most challenging areas due to additional illumination from other wave energy besides primary reflections, such as multiples and diving waves, and the least-squares data-fitting process that balances the amplitude and attenuates migration noise. However, FWI velocity models can be contaminated by crosstalk noise among different wave modes or different physical parameters; therefore, the interpretation of FWI images should be performed with care.

FWI imaging updates the velocity and obtains a reflectivity image in one (iterative) inversion. This means that it requires resolving both low wavenumbers and high wavenumbers of the earth model. However, as the high-frequency component of the velocity model has almost no impact on the kinematics, the accuracy of low- to mid-frequency velocity remains key to improving the imaging, either for conventional migrations or FWI imaging. As shown in Figure 8, although the first-round 7 Hz TLFWI update on top of a legacy model (Figure 8a) shows good improvements in the corresponding FWI image (as indicated by the green arrow in Figure 8d) over the legacy RTM (Figure 8b), a large area still has very poor image quality (red ellipse in Figure 8d). This is due to the large salt model errors in the FWI input and the insufficient data constraints provided by the staggered-shot streamer data for FWI to correct for such errors. With iterative salt scenarios that use prior rounds of FWI updates as a hint to build a better initial model for the next round, FWI is finally able to better resolve the complex salt geometry in the overburden (Figure 8e) and reveals images directly below (green ellipse in Figure 8f). However, salt scenario testing, even if guided by FWI updates, is often a game of hit or miss. Therefore, in areas of complex geology, we still need better data with lower frequencies and wider offsets that can provide better constraints for FWI (Dellinger et al., 2016).

When a reasonably accurate background model is obtained from low-frequency inversion, FWI imaging at high frequencies is a more linear problem than at low frequencies. In this regard, high-frequency FWI imaging is similar to LSM in that both invert for a reflectivity image through a least-squares data-fitting
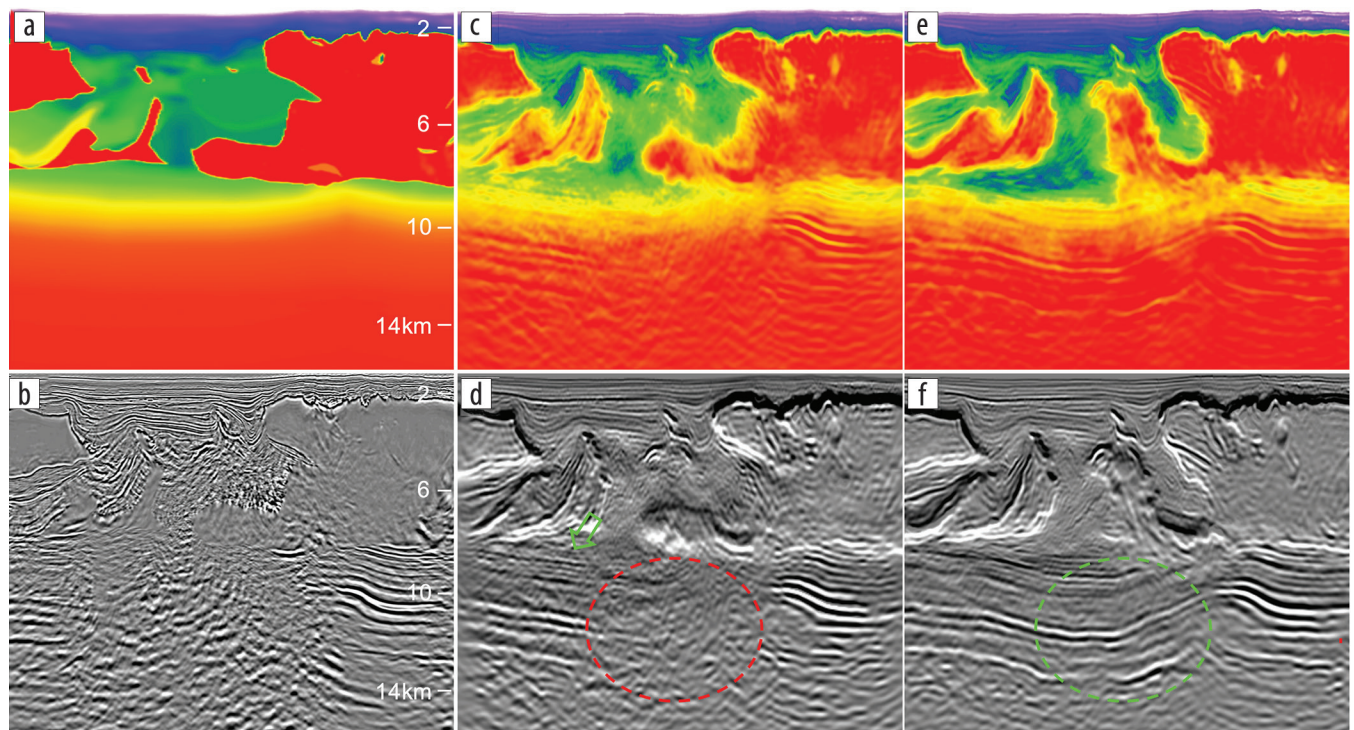

Figure 8. Improved velocity model and image after iterative scenarios and TLFWI updates for a staggered-shot streamer data set (Mandroux et al., 2013) with 10 km full-azimuth offset and 18 km maximum offset in the GoM. Panel (a) is the legacy model, and (b) is the corresponding 15 Hz RTM image. Panel (c) is the 7 Hz TLFWI model started from the legacy model, and (d) is its corresponding FWI image. Panels (e) and (f) show the improved 7 Hz TLFWI model and FWI image, respectively, after iterations of scenarios and TLFWI updates.

process. However, FWI imaging is quite different from LSM. First, while LSM normally only uses the processed primary reflections as input data, FWI imaging uses the full-wavefield data, which gives FWI imaging additional illumination power over LSM. Second, as FWI imaging uses full-wavefield modeling rather than Born modeling as used in LSM, the transmission effect is better simulated in FWI imaging, which potentially allows for better illumination compensation. Third, unlike LSM that only runs inversion at the maximum frequency, FWI imaging inverts from low to high frequency, which facilitates a full extraction of information at different length scales from the input seismic data. The benefit of FWI imaging over LSM can be observed in Figure 9 where the FWI image (Figure 9c) shows better low-frequency components (as indicated by the yellow ellipse) and better compensated amplitudes (as indicated by the yellow arrow) compared to LSM (Figure 9b).

If FWI can obtain a correct velocity model and if the assumption of density (constant, or a smooth function, or more generally proportional to the velocity) holds, the FWI image should carry reasonably good amplitudes as well. To evaluate the amplitudes of

the FWI image, we extracted the trough amplitude of the main reservoir from the 18 Hz RTM image (Figure 10a) and 18 Hz FWI image (Figure 10b) from the Atlantis OBN survey. The amplitudes of the RTM image and FWI image are comparable overall in the area outboard of salt. Whereas, for the subsalt portion of the reservoir, the amplitude extraction from the FWI image shows a much better definition of the reservoir extension and the oil-water contact as confirmed by wells. The observation here shows that the amplitudes of the FWI image are more reliable than those of the RTM image, especially in weak illumination zones. However, there are cases where density is in the opposite trend to velocity and happens to dominate the impedance contrast. For those areas, the amplitude and phase of the FWI image would be in doubt even if we were able to obtain an accurate velocity. Incorporating density into the inversion would be needed to solve this problem.

Although the FWI image, as the spatial derivative of FWI velocity in the normal direction, provides a higher-frequency image that is better for structure mapping, velocity itself is often a valuable attribute for direct interpretation. As shown in Figure 11, the baffle between the two reservoirs (yellow arrows) can be better inferred on the FWI image (Figure 11b) compared to the Q-Kirchhoff image (Figure 11a) based on the relative amplitudes; however, it is the larger velocity values in the baffle area that provide a more confident interpretation of two isolating reservoirs. Of course, more in-depth interpretation of rock properties for prospecting and reservoir analysis would require elastic parameters such as V_P, V_S, and density. In conventional migrations, elastic parameters can be derived through amplitude variation with angle inversion of the gathers output from migration. To achieve the same goal in the framework of FWI imaging, we could formulate the inversion to output the angle-dependent
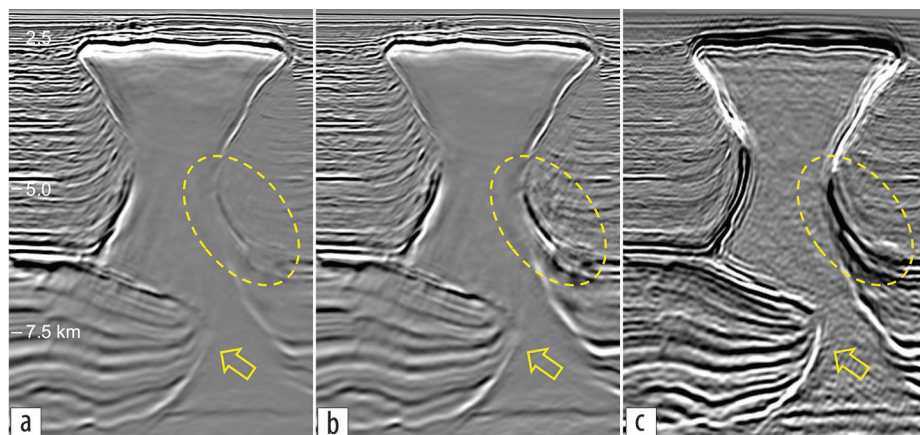

Figure 9. Section view of (a) 20 Hz RTM, (b) 20 Hz LSRTM, and (c) 20 Hz FWI image at Herschel OBN (Yao et al., 2020) in the GoM. The FWI image shows better low-frequency components and better compensated amplitudes compared to LSRTM. Note that the LSRTM result shown here is obtained from single-iteration image-domain LSM.
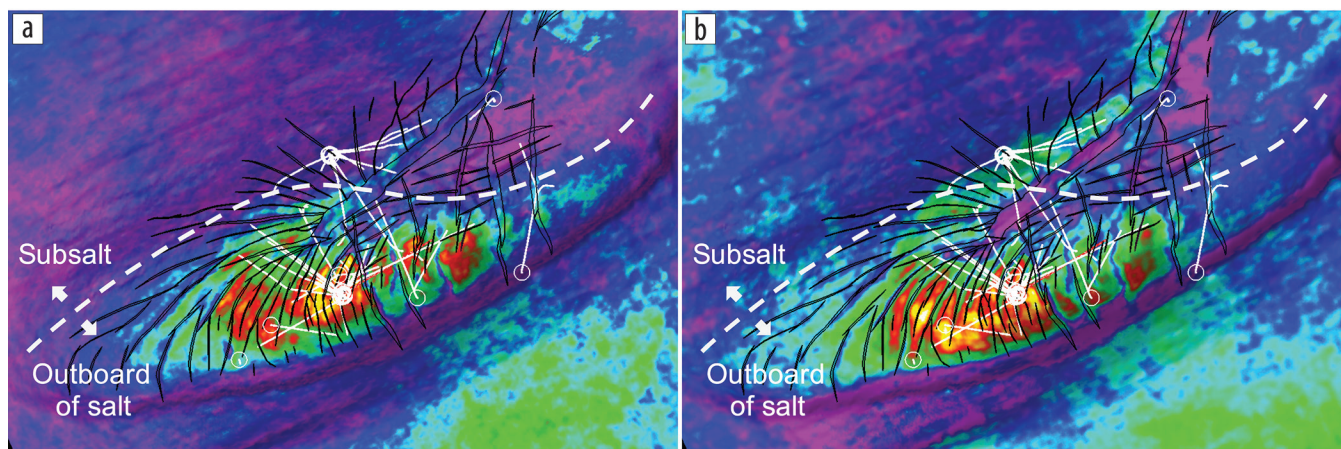

Figure 10. Trough amplitude at the main reservoir from (a) the 18 Hz RTM image and (b) the 18 Hz FWI image from Atlantis OBN as shown in Figures 1–3. Black polygons indicate the interpretation of fault blocks, and white solid lines show the well paths. Comparable amplitude between the RTM image and FWI image is observed at the area outboard of salt, while the FWI image provides a better definition of the subsalt portion of the reservoir.
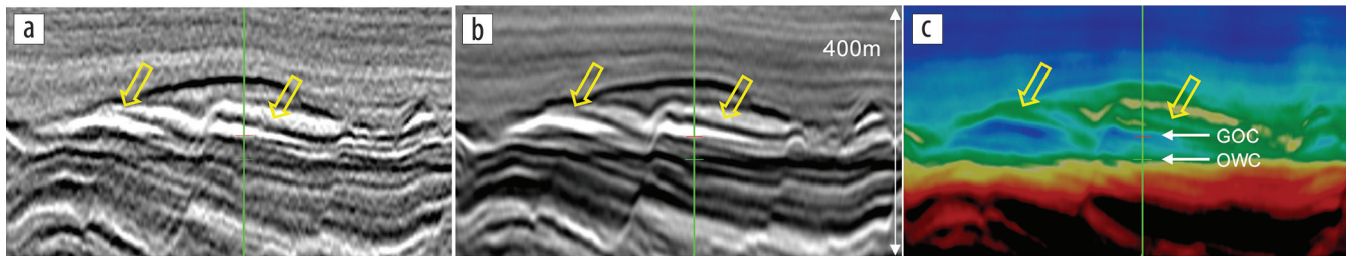
Special Section: Seismic imaging below complex overburdens

Figure 11. A close-up view around a reservoir interval from the same Barents Sea source-over-spread NATS data set as shown in Figure 5 with (a) 100 Hz Q-Kirchhoff, (b) 48 Hz FWI image, and (c) the corresponding 48 Hz TLFWI model. The green vertical line indicates the well path, and the two yellow arrows indicate two confirmed reservoirs. Red and green horizontal markers refer to gas-oil contact (GOC) and oil-water contact (OWC), respectively. Although the baffle separating the two reservoirs can be better interpreted on the FWI image compared to the Q-Kirchhoff result based on the relative amplitudes, the TLFWI velocity provides a more confident interpretation given the larger velocity values in the baffle area.

reflectivity, or push toward the direction of multiparameter elastic FWI that directly outputs the elastic parameters.

Based on the learnings noted in this paper, several approaches can be taken to further improve FWI imaging. On the acquisition side, we can push for new surveys with lower frequencies and wider offsets that are more favorable for FWI to improve the low-wavenumber model for better kinematics. On the algorithm side, we can incorporate more physics into the FWI modeling engine and inversion scheme to reduce crosstalk among different wave modes or different physical parameters and eventually move toward elastic FWI with multiparameter inversion. At the same time, we need to improve the efficiency of the algorithm to make FWI feasible for even larger apertures, even higher frequencies, and more accurate physics.

Last but not least, FWI imaging requires no preprocessing and migration. Although there are still potential issues in FWI images as discussed earlier, an FWI image at the current state of the art is already an attractive fast-track product and, at the minimum, is a complement to conventional migration images, ready for subsurface mapping in just a few weeks after input data are available. We note that FWI and thus FWI imaging require a reasonably good initial model. Therefore, conventional VMB workflows may still be needed when a velocity model is unavailable or not sufficiently accurate.

Conclusions

The advancement of FWI algorithms and high-performance computing allows us to finally realize full-wavefield imaging through FWI. FWI imaging has been applied successfully to various data types in different geologic settings, solving some of the most challenging imaging problems that cannot be resolved with conventional migrations. Just as FWI has revolutionized the VMB workflow in recent years, FWI imaging has opened the door to another paradigm shift in seismic imaging. **TLE**

Acknowledgments

We thank BP, BHP, TGS, and CGG for permission to publish this work. We are also grateful to numerous CGG colleagues for successfully applying the FWI imaging workflow to different data sets.

Data and materials availability

Data associated with this research are confidential and cannot be released.

Corresponding author: rongxin.huang@cgg.com

References

Baysal, E., D. D. Kosloff, and J. W. C. Sherwood, 1983, Reverse time migration: Geophysics, **48**, no. 11, 1514–1524, https://doi.org/10.1190/1.1441434.

Berkhout, A. J., 2012, Combining full wavefield migration and full waveform inversion, a glance into the future of seismic imaging: Geophysics, **77**, no. 2, S43–S50, https://doi.org/10.1190/geo2011-0148.1.

Claerbout, J. F., 1971, Toward a unified theory of reflector mapping: Geophysics, **36**, no. 3, 467–481, https://doi.org/10.1190/1.1440185.

Dellinger, J., A. Ross, D. Meaux, A. Brenders, G. Gesoff, J. Etgen, J. Naranjo, G. Openshaw, and M. Harper, 2016, Wolfspar®, an "FWI-friendly" ultralow-frequency marine seismic source: 86th Annual International Meeting, SEG, Expanded Abstracts, 4891–4895, https://doi.org/10.1190/segam2016-13762702.1.

Etgen, J., S. H. Gray, and Y. Zhang, 2009, An overview of depth imaging in exploration geophysics: Geophysics, **74**, no. 6, WCA5–WCA17, https://doi.org/10.1190/1.3223188.

Lailly, P., 1983, The seismic inverse problem as a sequence of before stack migrations: Conference on Inverse Scattering: Theory and application, SIAM, 206–220.

Lewis, B., C. Brooks, M. Pfister, S. Michell, and G. Astvatsaturov, 2016, Efficient acquisition of deepwater node surveys: 86th Annual International Meeting, SEG, Expanded Abstracts, 92–96, https://doi.org/10.1190/segam2016-13867668.1.

Liu, Y., X. Chang, D. Jin, R. He, H. Sun, and Y. Zheng, 2010, Reverse time migration of multiples for subsalt imaging: Geophysics, **76**, no. 5, WB209–WB216, https://doi.org/10.1190/geo2010-0312.1.

Loewenthal, D., L. Lu, R. Roberson, and J. Sherwood, 1976, The wave equation applied to migration: Geophysical Prospecting, **24**, no. 2, 380–399, https://doi.org/10.1111/j.1365-2478.1976.tb00934.x.

Lu, R., 2016, Revealing overburden and reservoir complexity with high-resolution FWI: 86th Annual International Meeting, SEG, Expanded Abstracts, 1242–1246, https://doi.org/10.1190/segam2016-13872562.1.

Lu, S., N. D. Whitmore, A. A. Valenciano, and N. Chemingui, 2011, Imaging of primaries and multiples with 3D SEAM synthetic: 81st Annual International Meeting, SEG, Expanded Abstracts, 3217–3221, https://doi.org/10.1190/1.3627864.

Mandroux F., C.-O. Ting, B. Montgomery, and A. Lenart, 2013, Staggered marine acquisition design for complex imaging: 83rd Annual International Meeting, SEG, Expanded Abstracts, 26–30, https://doi.org/10.1190/segam2013-0354.1.

Michell, S., X. Shen, A. Brenders, J. Dellinger, I. Ahmed, and K. Fu, 2017, Automatic velocity model building with complex salt: Can computers finally do an interpreter's job?: 87th Annual International

Meeting, SEG, Expanded Abstracts, 5250–5254, https://doi.org/10.1190/segam2017-17778443.1.

Nemeth, T., C. Wu, and G. T. Schuster, 1999, Least-squares migration of incomplete reflection data: Geophysics, **64**, no. 1, 208–221, https://doi.org/10.1190/1.1444517.

Roberts, M., T. Dy, S. Ji, M. Reasnor, and D. Shepherd, 2011, Improving Atlantis TTI model building: OBN+NATS, prism waves and 3D RTM angle gathers: 81st Annual International Meeting, SEG Expanded Abstracts, 3238–3242, https://doi.org/10.1190/1.3627868.

Shen, X., I. Ahmed, A. Brenders, J. Dellinger, J. Etgen, and S. Michell, 2017, Salt model building at Atlantis with full-waveform inversion: 87th Annual International Meeting, SEG, Expanded Abstracts, 1507–1511, https://doi.org/10.1190/segam2017-17738630.1.

Shen, X., L. Jiang, J. Dellinger, A. Brenders, C. Kumar, M. James, J. Etgen, D. Meaux, R. Walters, and N. Abdullayev, 2018a, High resolution full-waveform inversion for structural imaging in exploration: 87th Annual International Meeting, SEG, Expanded Abstracts, 1098–1102, https://doi.org/10.1190/segam2018-2997202.1.

Shen, X., I. Ahmed, A. Brenders, J. Dellinger, J. Etgen, and S. Michell, 2018b, Full-waveform inversion: The next leap forward in subsalt imaging: The Leading Edge, **37**, no. 1, 67b1–67b6, https://doi.org/10.1190/tle37010067b1.1.

Sirgue, L., O. I. Barkved, J. P. Van Gestel, O. J. Askim, and J. H. Kommedal, 2009, 3D waveform inversion on Valhall wide-azimuth OBC: 71st Conference and Exhibition, EAGE, Extended Abstracts, https://doi.org/10.3997/2214-4609.201400395.

Tarantola, A., 1984, Inversion of seismic reflection data in the acoustic approximation: Geophysics, **49**, no. 8, 1259–1266, https://doi.org/10.1190/1.1441754.

Tarantola, A., 1986, A strategy for nonlinear elastic inversion of seismic reflection data: Geophysics, **51**, no. 10, 1893–1903, https://doi.org/10.1190/1.1442046.

Verschuur. D. J., A. J. Berkhout, and C. P. A. Wapenaar, 1992, Adaptive surface-related multiple elimination: Geophysics, **57**, no. 9, 1166–1177, https://doi.org/10.1190/1.1443330.

Vinje, V., J. E. Lie, V. Danielsen, P. E. Dhelie, R. Silliqi, C.-I. Nilsen, E. Hicks, and A. Camerer, 2017, Shooting over the seismic spread: First Break, **35**, no. 6, 97–104, https://doi.org/10.3997/1365-2397.35.6.89461.

Virieux, J., and S. Operto, 2009, An overview of full-waveform inversion in exploration geophysics: Geophysics, **74**, no. 6, WCC1–WCC26, https://doi.org/10.1190/1.3238367.

Wang, P., S. Ray, C. Peng, Y. Li, and G. Poole, 2013, Premigration deghosting for marine streamer data using a bootstrap approach in tau-p domain: 83th Annual International Meeting, SEG, Expanded Abstracts, 4221–4225, https://doi.org/10.1190/segam2013-0225.1.

Wang, P., Z. Zhang, J. Mei, F. Lin, and R. Huang, 2019, Full-waveform inversion for salt: A coming of age: The Leading Edge, **38**, no. 3, 304–213, https://doi.org/10.1190/tle38030204.1.

Wong, M., B. Biondi, and S. Ronen, 2014, Imaging with multiples using least-squares reverse time migration: The Leading Edge, **33**, no. 9, 970–976, https://doi.org/10.1190/tle33090970.1.

Yang, Z., J. Hembd, H. Chen, and J. Yang, 2015, Reverse time migration of multiples: Applications and challenges: The Leading Edge, **34**, no. 7, 780–784, https://doi.org/10.1190/tle34070780.1.

Yao, Y., H. Zhang, L. Hu, and C. Peng, 2020, Improving Mississippi Canyon images with ocean bottom node data: Challenges and surprises: 90th Annual International Meeting, SEG, Expanded Abstracts, 661–665, https://doi.org/10.1190/segam2020-3423896.1.

Zhang, Z., J. Mei, F. Lin, R. Huang, and P. Wang, 2018, Correcting for salt misinterpretation with full-waveform inversion: 88th Annual International Meeting, SEG, Expanded Abstracts, 1143–1147, https://doi.org/10.1190/segam2018-2997711.1.

Zhang, Z., Z. Wu, Z. Wei, J. Mei, R. Huang, and P. Wang, 2020, FWI imaging: Full-wavefield imaging through full-waveform inversion: 90th Annual International Meeting, SEG, Expanded Abstracts, 656–660, https://doi.org/10.1190/segam2020-3427858.1.